Supporting Information Available.

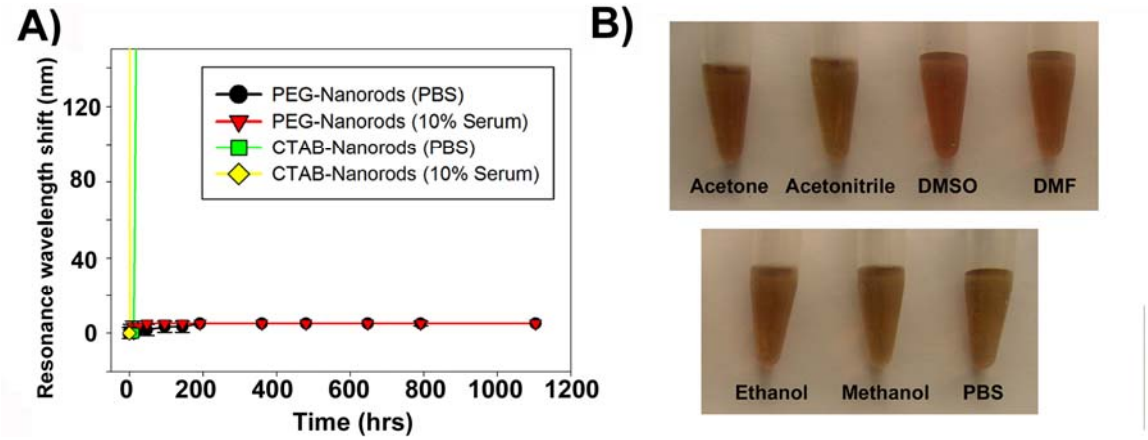

Supplementary Figure 1: *PEG-Nanorod Synthesis and Stability In Vitro.* A) The plasmon resonance of gold nanomaterials is highly sensitive to aggregation-mediated red-shifting. By monitoring plasmon resonance peak over >1000 hrs in biological solutions, we find that PEG-nanorods show prolonged stability in biological media while CTAB-coated nanorods aggregated over time in PBS (0.15 M NaCl 0.1 M Na Phosphate, pH 7.2) or 10% human serum monitored for over 1000 hrs *in vitro*. B) PEG-NRs were readily dispersed in a variety of solvents, including acetone, acetonitrile, dimethyl sulfoxide (DMSO), dimethylformamide (DMF), ethanol, methanol, or PBS.

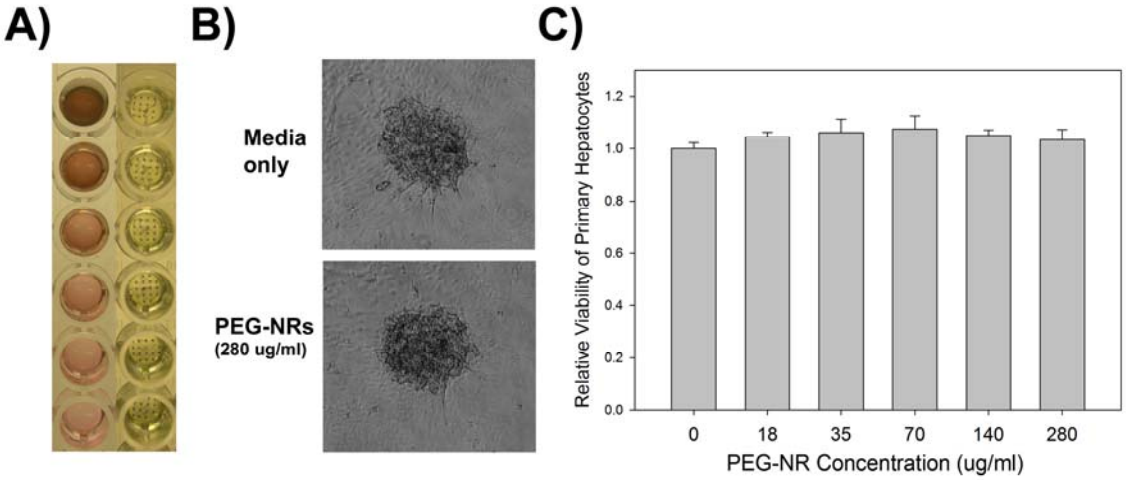

Supplementary Figure 2: *Probing Nanorod Cytotoxicity to Primary Rat Hepatocyte cocultures.* A) Primary rat hepatocyte: 3T3-J2 human fibroblast co-cultures were incubated with PEG-NRs at varying concentrations for 24 hrs (left column), rinsed, and incubated with media containing thiazolyl blue tetrazolium bromide (MTT reagent) at 0.5 mg/ml. After 1hr, blue precipitates begin to form within hepatocytes as a result of mitochondrial activity (right column). B) Microscopy shows cultures incubated with PEG-NRs at maximal concentrations to show similar morphology to controls. C) Quantitaion of cellular viability via absorbance of DMSO:isopropanol-solubilized MTT reagent shows no cytotoxicity of PEG-NRs, even at concentrations of 20-times that used *in vitro* here and approximately equal to maximum blood concentrations during *in vivo* experiments.

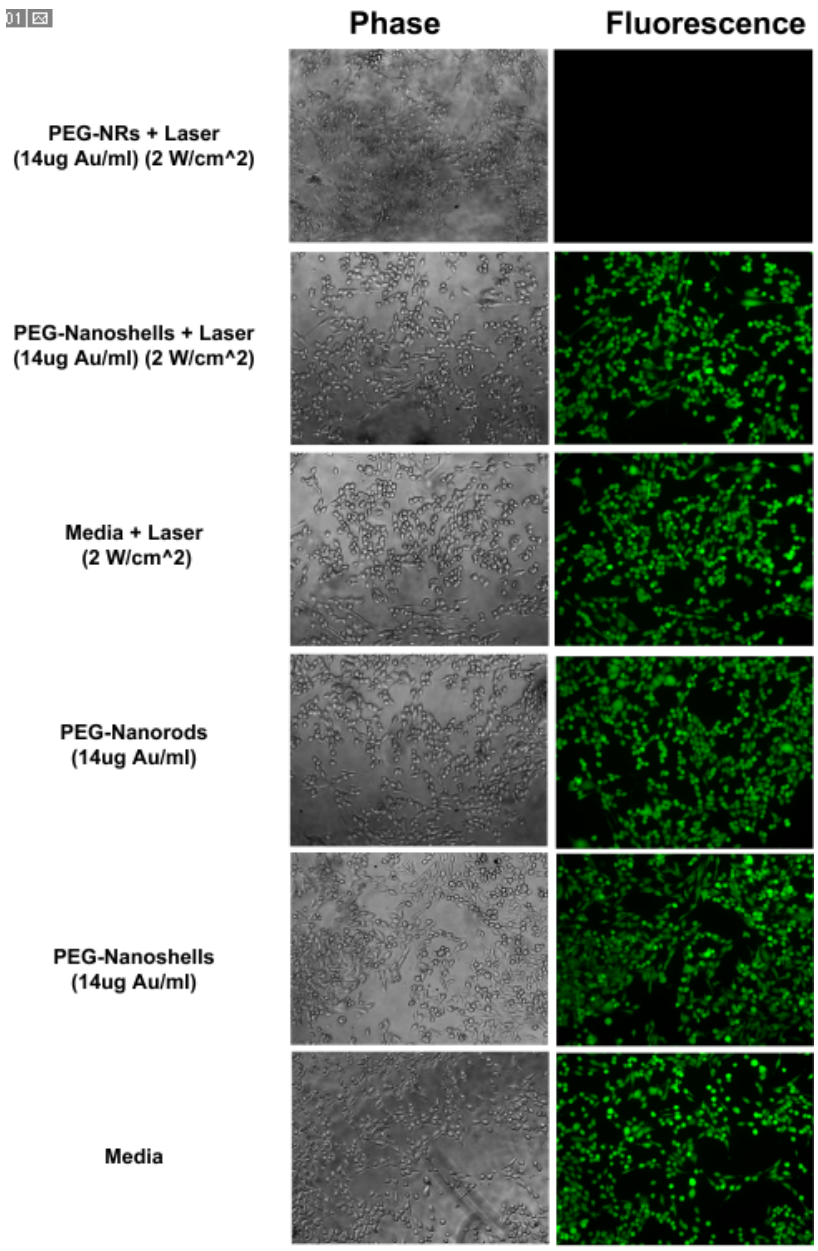

Supplementary Figure 3: *Probing Photothermal PEG-Nanorod Cytotoxicity to MDA-MB-435 Tumor Cell Cultures Compared to PEG-Nanoshells.* Human tumor cell cultures (MDA-MB-435) were incubated with PEG-Nanorods (14 μg/ml), PEG-Nanoshells (14 μg/ml), or media and irradiated at 2 W/cm^2 for 5 min. Following irradiation, cells were washed and incubated with Calcein AM, a fluorogenic esterase substrate, to detect cell viability. Irradiation of PEG-Nanorods leads to photothermal destruction of cells, while controls and PEG-Nanoshells show high cell viability.

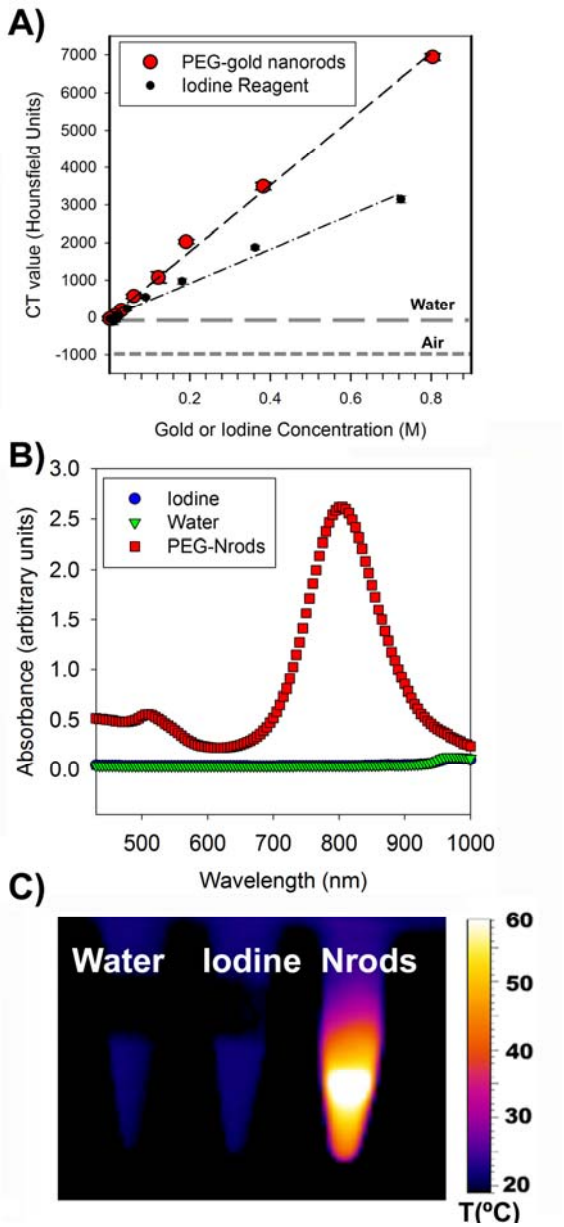

Supplementary Figure 4: *X-ray Absorption, Optical Spectra, and Photothermal Comparison between PEG-Nanorods and Clinical Iodine X-ray Computed Tomography Reagent.* A) X-ray computed tomography number of PEG-nanorods compared to an iodine standard (Isovue-370). Linear x-axis plot of the same data presented in Figure 2B, clarifying linearity of PEG-gold nanorod detection via x-ray CT B) Optical extinction spectra of PEG- Nanorods (0.045 mg/ml Au) vs solution of an iodine-based clinical regent (350 mg/ml iodine) and saline. Notably, iodine reagents lack absorbance in the near-infrared that could allow remote photothermal heating. B) Photothermal heating comparison between PEG-Nanorods, iodine, and saline monitored using infrared thermography (810 nm NIR light, 2 W/cm^2).

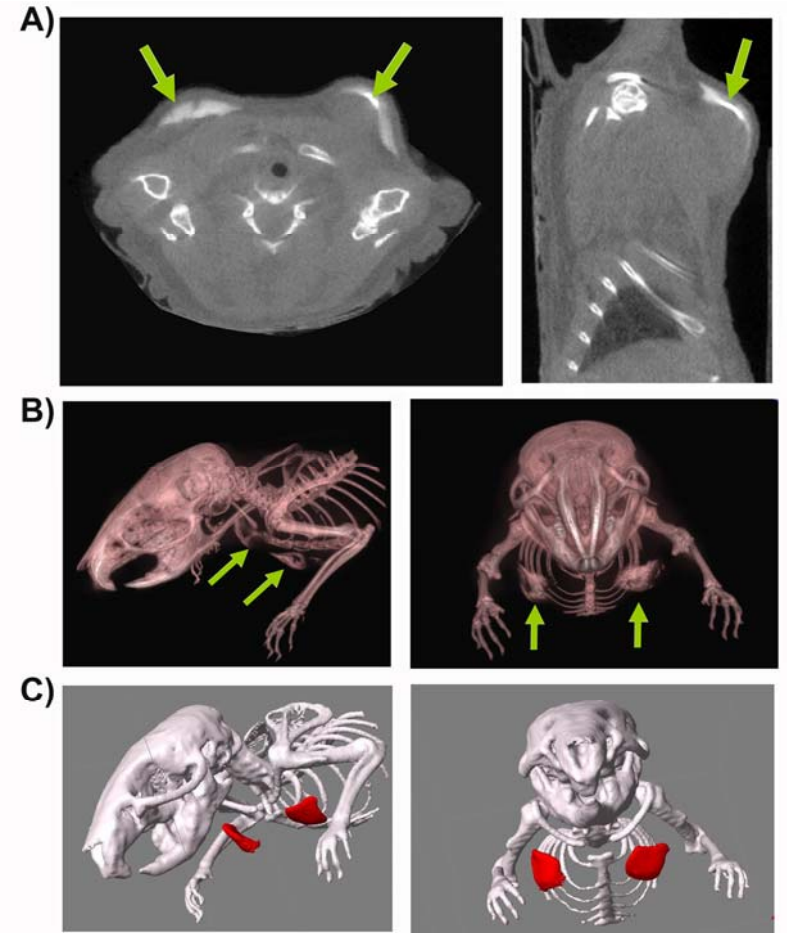

Supplementary Figure 5: *Linking PEG-Nanorod X-ray Tomography with Computational Modeling.* A) Transverse and sagittal slices showing PEG-Nanorod distributions following intratumoral administration into bilateral breast tumors B) 3D reconstructions depicting geometry of PEG-NR injections C) Importation of 3D x-ray CT data into geometries for 4D photothermal modeling (red= PEG-nanorods, white=skeletal structure).

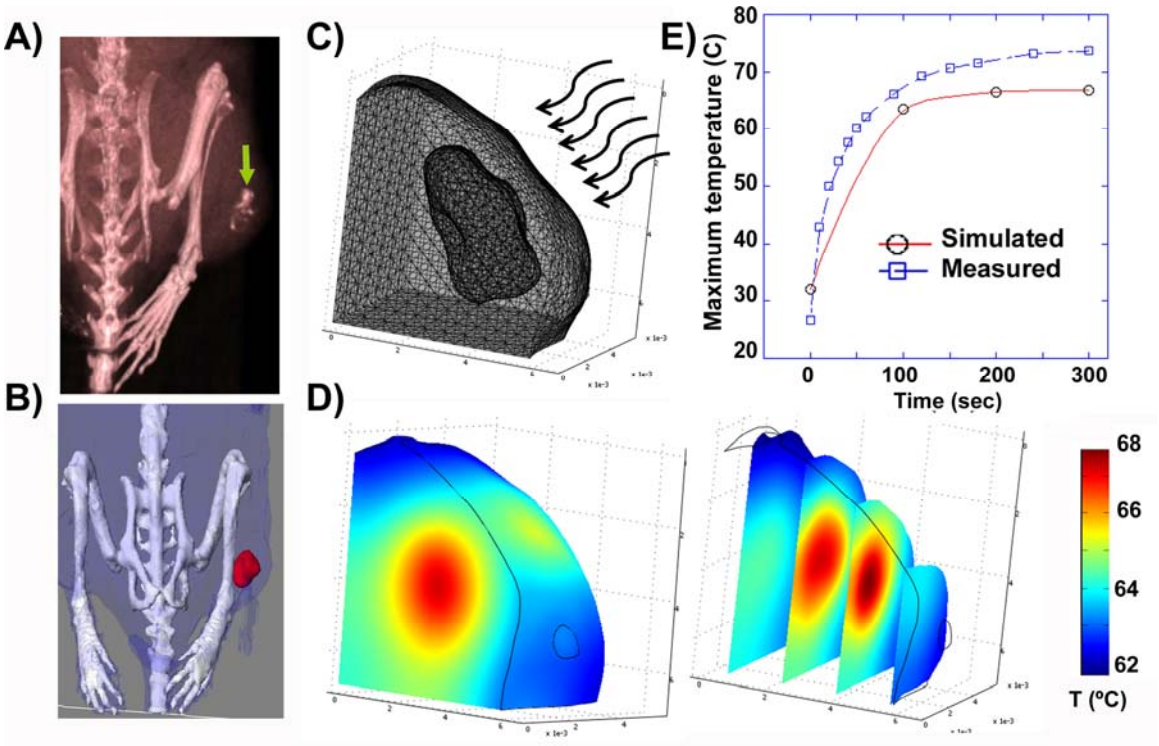

Supplementary Figure 6: *X-ray CT-Fused Computational Modeling of Photothermal Tumor Heating.* A) X-ray CT image of PEG-Nanorod distribution in tumor B) A 3D solid model of the complete geometry was reconstructed by image processing for use with computational photothermal modeling. C) Meshed geometry of the injected tumor chosen as the computational domain with laser orientation and intensity matching that used (1 W/cm^2) (laser direction signified by curved arrows) D) Plot of theoretical surface temperature distribution (left) and the internal predicted temperature profiles inside the computational geometry of the tumor (right) 240 sec following the onset of irradiation. E) Graphical comparison between simulated and thermographically measured maximum surface temperatures over time after the onset of irradiation.

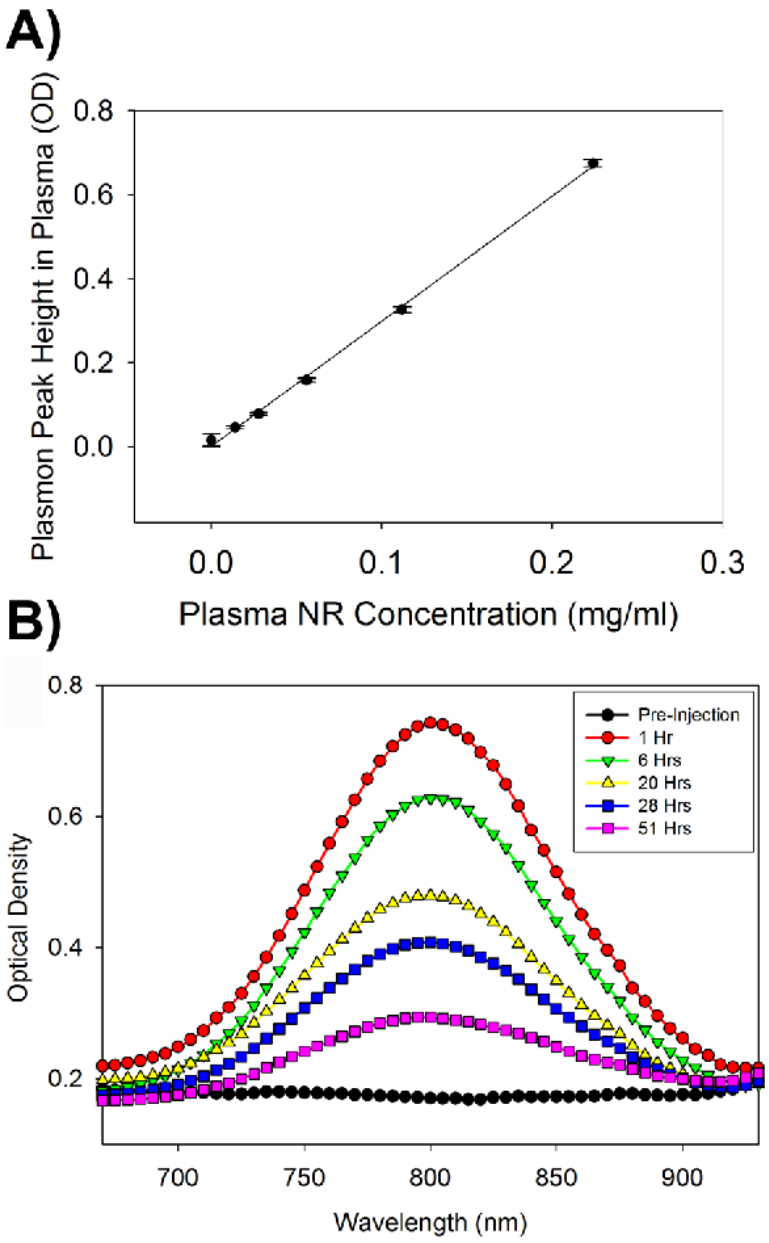

Supplementary Figure 7: *Assessing PEG-NR concentration in plasma via plasmon resonance peak height.* A) PEG-NRs at various concentration were diluted into plasma and spectrophotometrically analyzed to assess NR concentration via the NIR plasmon resonance peak. NRs could be rapidly quantified between ~0.2 mg/ml (the approximate concentration in plasma immediately following injection in mice) and ~0.02 mg/ml. B) Following injection, this method could be applied to rapidly detect PEG-NRs in the plasma of injected mice over time, showing that PEG-NRs maintain their plasmon resonance throughout their blood circulation *in vivo*.

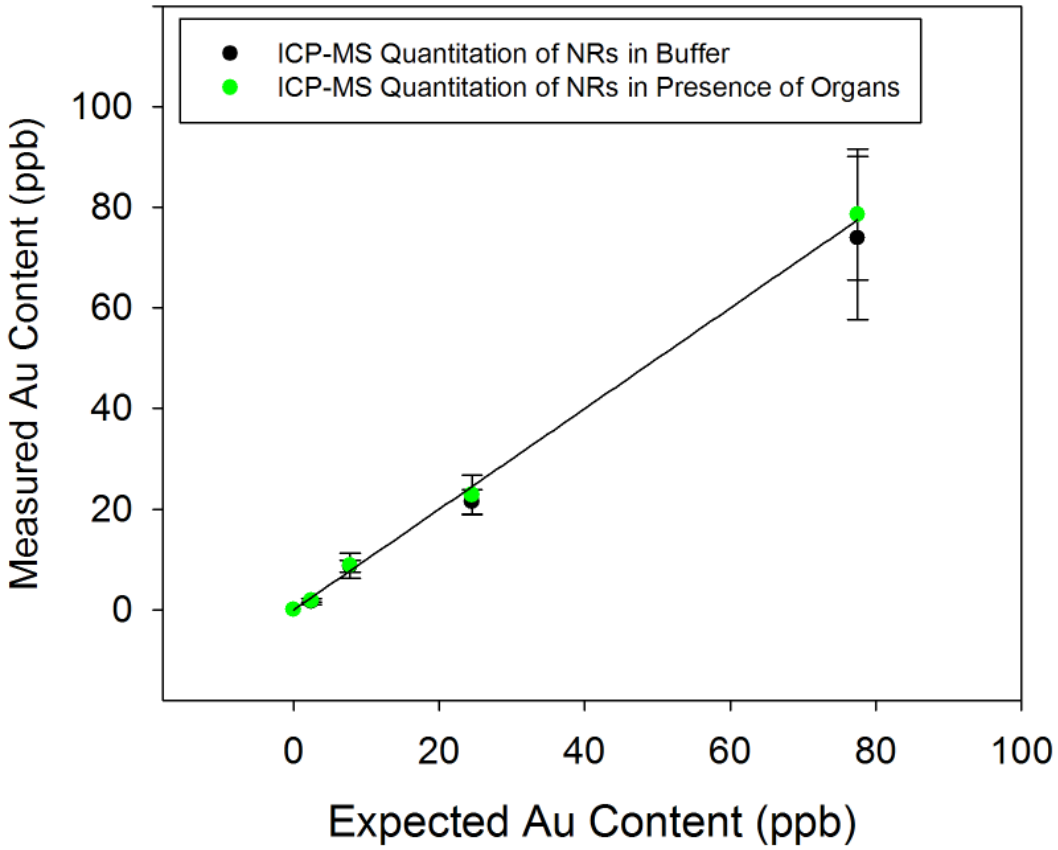

Supplementary Figure 8: *Assessing PEG-NR concentration in organs via ICP-MS Au quantitiation.* PEG-NRs at various concentration were diluted into buffer or into glass vials containing 200 mg sections of liver. Samples were all prepared for ICP-MS quantitation to assess the linearity of Au detection and whether the presence of organs affected quantitation. The samples were made to approximate a range of ~2% to 70% ID/g for 200 mg tissues. Results are plotted for triplicate samples and plotted against the ideal relationship of y=x.

Supplemental Table 1. *Tabular Representation of PEG-NR Biodistribution Data from Figure 5B.*

Tissue	% ID / gram tissue	Standard Deviation
tumor	7.1	+/- 2.9
brain	0.5	+/- 0.3
bladder	0.4	+/- 0.1
muscle	1.7	+/- 0.8
heart	2.4	+/- 0.9
lung	4.4	+/- 0.9
kidney	4.0	+/- 0.3
liver	14.0	+/- 4.0
spleen	51.9	+/- 13.0

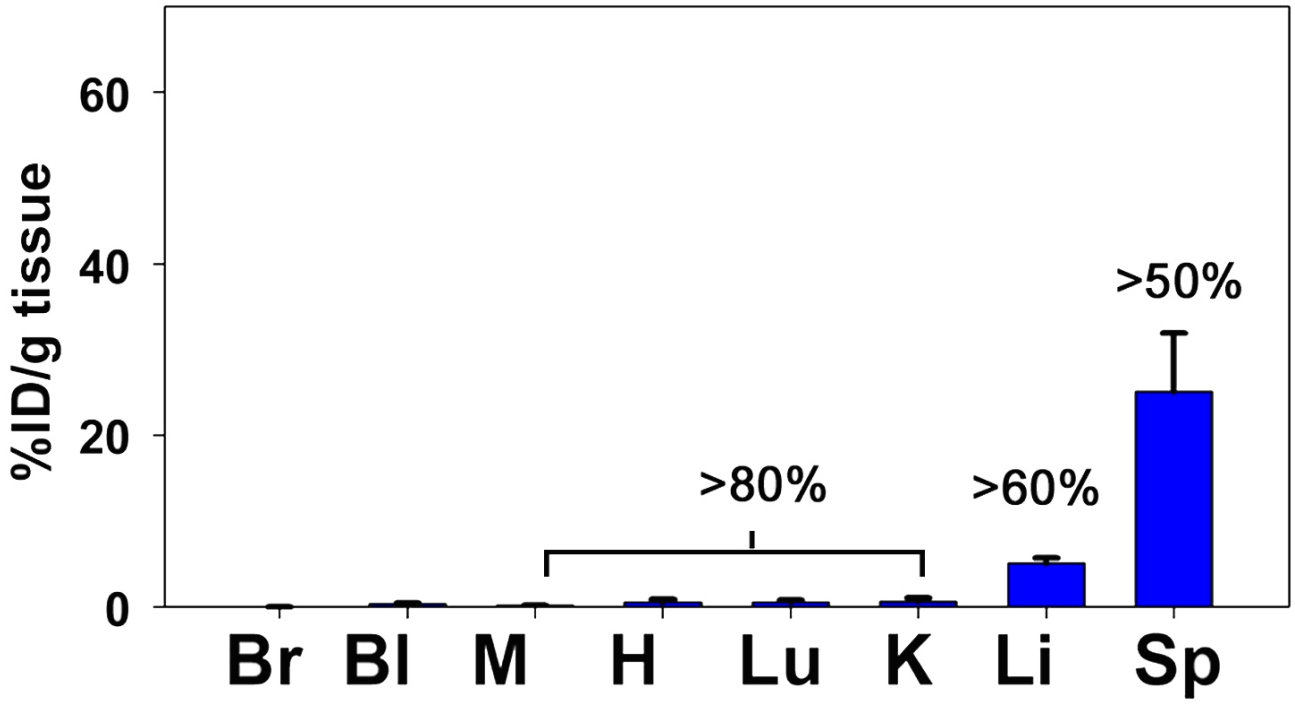

Supplementary Figure 9: *PEG-NR biodistribution in tumor-free mice at 2 months following intravenous injection.* PEG-nanorod biodistribution 2 months following intravenous administration, quantified via ICP-MS (3 mice). Percent values indicate the clearance (or decrease in %ID/g) that occurred during this time period compared to values of organs collected 72 hrs after particle injection (Br=brain, Bl=bladder, M=muscle, H=heart, Lu=lung, K=kidney, Li=liver, Sp=spleen).

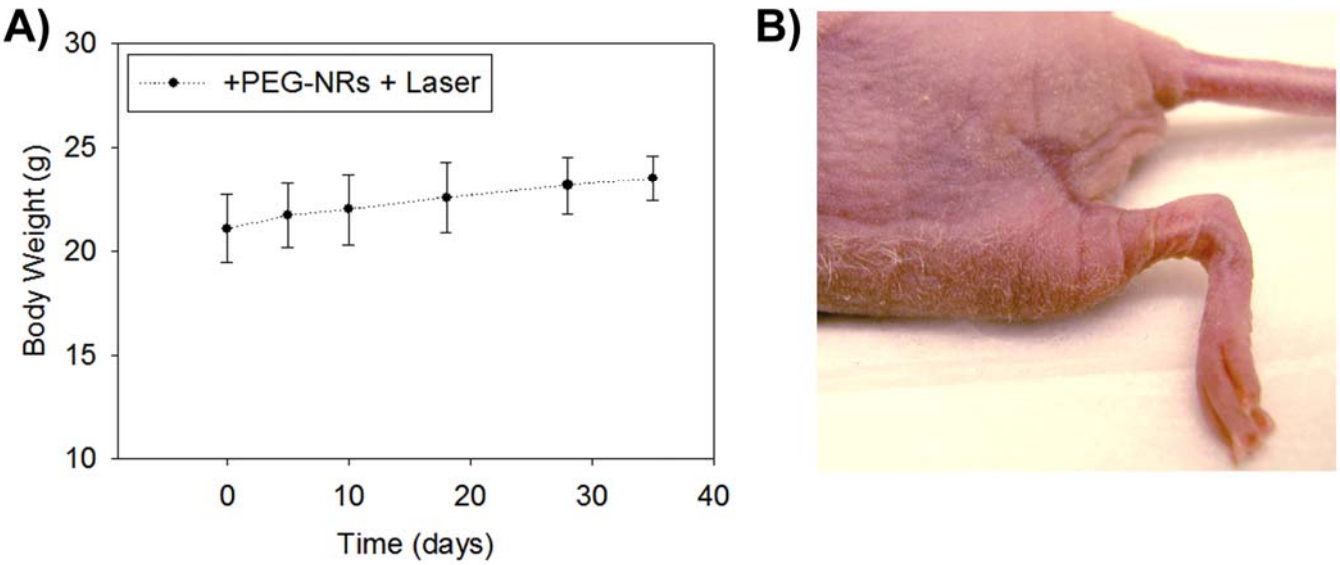

Supplementary Figure 10: *Weight of irradiated, PEG-NR-injected mice during tumor resorption following treatment.* A) Body weight curve of mice bearing unilateral MDA-MB-435 tumors from the survival study (Figure 5C). No obvious body weight loss was observed following PEG-NR-mediated tumor therapy. C) Close view of site of tumor resportion showing only evidence of minor scar.

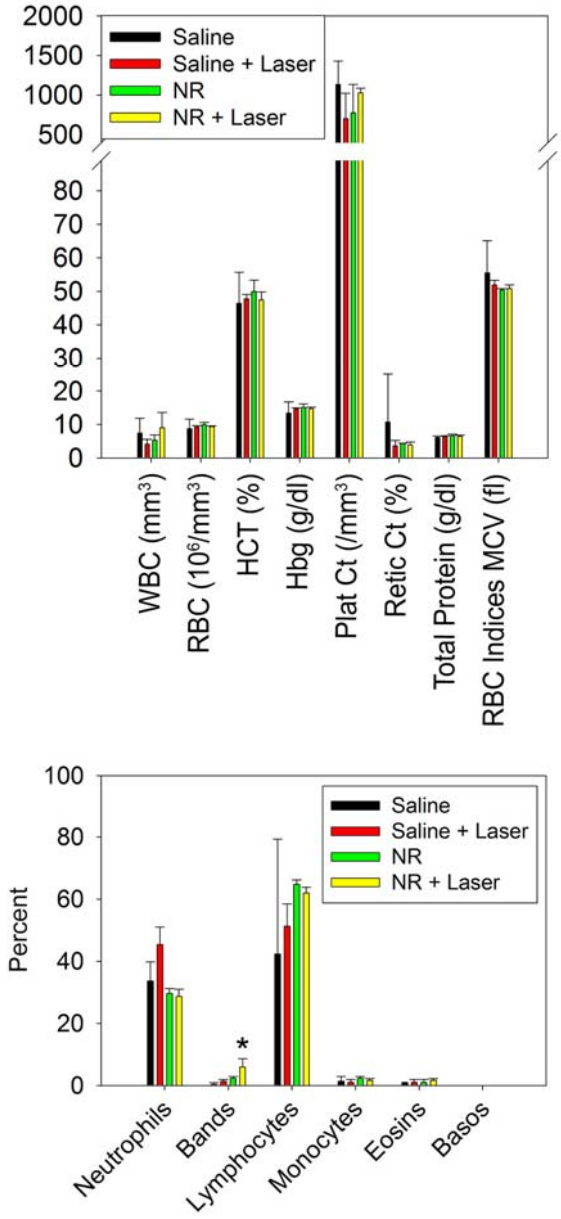

Supplementary Figure 11: *Hematological effects of PEG-NR irradiation in mice.* To explore the effects of NR administration and near-infrared ablation, mice bearing bilateral MDA-MB-435 tumors were injected with either saline or PEG-NRs and, 72 hrs later, either exposed to the therapeutic tumor irradiation protocol under anaesthetic (~2 W/cm^2, 5 min, 810 nm) or anaesthetized without irradiation (n=3 each set). Following irradiation or comparable time under anaesthetic, blood was collected for hematology and mice were sacrificed. The only statistically-significant change observed in response to NR-mediated tumor ablation was a slight increase in the percent of band neutrophils ($p<0.05$ for NR+ Laser vs NR, Saline + Laser, and Saline), likely due to an acute inflammatory response to tumor ablation.

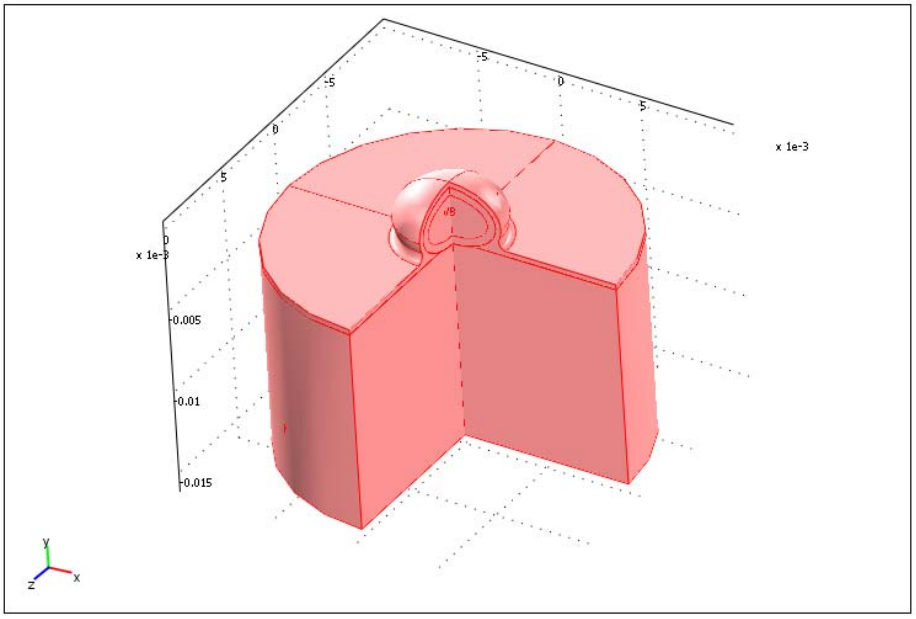

Supplementary Figure 12: *Compuatational domain for modeling photothermal therapy following intravenous administration of PEG-Nanorods.* For intravenous photothermal modeling, a cylindrical domain of 20 mm diameter around the tumor with a depth of 12 mm for the muscle domain was considered for computation. The outer shell of the tumor was considered to be of 0.5 mm thickness.

Finite Element Modeling of Photothermal Tumor Heating

To reveal the magnitude and kinetics of *in vivo* photothermal heat generation by the nanorods and native tissue, the temporal and spatial propagation of thermal gradients, and to assess the timescale within which the entire tumor volume would reach ablative temperatures, a finite element computer simulation of the photothermal ablation process was developed and carried out. The tumor was approximated as a paraboloid, resting above the muscle and covered by skin of 300 μm thickness. The bio-heat transfer equation of Pennes (1948) was applied to the computational domain in the form:

$$\rho c\,(\partial T/\partial t) + \nabla . (-k \nabla T) = \rho_b c_b w_b (T_b - T) + Q_{met} + Q_{laser}$$

Where, ρc is the heat capacity of the muscle, tumor periphery, tumor core or skin as appropriate in the respective regions. The heat capacity of blood is $\rho_b c_b$ and its perfusion rate in the respective domain is w_b. Q_{met} and Q_{laser} are the metabolic and laser heat generation in the tissues respectively. For intravenous photothermal modeling, a cylindrical domain of 20 mm diameter around the tumor with a depth of 12 mm for the muscle domain was considered for computation. The shell of the tumor was considered to be of 0.5 mm thickness having higher rate of blood perfusion than the tumor core. A cut view of the computational domain is shown in Fig S10.

The blood perfusion rate is known to be different in tumor periphery, tumor core, healthy tissues and skin. Hence, they have been taken accordingly from literature (Fujita et al., 1998) as follows

$w_b = F\,[1]$ for $T < 39^0C$

$= F[1+ (p-1)\,(T-39)/(45-39)]$ for $39^0C < T < 45^0C$

$= F[p- (p-1)\,(T-45)/(51-45)]$ for $45^0C < T < 51^0C$

$= F\,[1]$ for $T > 51^0C$

The maximum perfusion rate and the parameter p for different region are given as

Tissue	F (m^3/kg/s)	p
Tumor core	5×10^{-7}	1
Tumor periphery	1.67×10^{-6}	2
Muscle	8.3×10^{-6}	9

Skin	8.3×10^{-6}	9

The thermophysical properties of various regions were taken from accepted values as

Tissue	Density	Specific heat	Thermal conductivity
	m^3/kg	J/(kgK)	W/(mK)
Tumor core	1050	3700	0.5
Tumor periphery	1050	3700	0.5
Muscle	1050	3700	0.5
Skin	1200	3700	0.2
Blood	1000	4200	-

The metabolic heat generation rate is taken to be 400 W/m^3.

Laser heat generation in tissues is a widely studied area. Welch (1984) gave a good overview of the various models available in this area. Seeing various possibilities, the following equation for heat generation, which is a modification of his equation (12) for the present geometry, was chosen:

$$Q_{laser} = \alpha I_0 \exp[-r^2/[2\sigma(0) \exp(\beta z_c)]]\exp[-(\alpha+\beta)z_c]$$

Where I_0 is the laser irradiation intensity in W/m^2, r is the radial distance from the center, and z_c is the depth of the location from the skin. The parameters α and β are the absorption and scattering coefficient (in m^{-1}) of the tissues respectively. To incorporate the curvature of the tumor's surface and the internal multi-layer tissue structure (skin, tumor), the following modification was made:

$$Q_{laser} = \alpha I_0 \exp[-r^2/[2\sigma(0) \exp(\beta z_c)]]\exp[-(\alpha+\beta)(z_c-c-d)] \exp[-(\alpha_s+\beta_s)(z_s)] \exp[-(\alpha_t+\beta_t)z_t]$$

Here, c is the depth of the skin surface from the tumor vertex at a given radial position, d is the depth of the normal tissue above a location, z_s is the depth of the skin above a location and z_t is the depth of the tumor tissue above a location. The suffixes: s and t indicate skin and tumor absorption and scattering

coefficients, respectively; the values of which were taken to be 0.4 and 5.3 cm^{-1} in absence of nanorods (Motamedi et al.(1983)). For the experiments with nanorods, the absorption coefficient of the tumor was predicted to be 3.07 cm^{-1} based on the Nrod biodistribution data (~7% ID/g; 20 mg/kg injected dose; 0.1 cm^3 tumor volume) and *in vitro* absorption measurements. Jain et al (2006) showed that the extinction coefficient of ~13 nm x 47 nm nanorods is dominated by absorption and hence we assumed that nanorods only enhance the tumor absorption coefficient, with insignificant alteration of large endogenous scattering coefficients. The surface heat loss coefficient to the environment was taken as 15 W/m^2K, which is a typical value for natural convection on planar surfaces.

Finite element method (FEM) using the multiphysics enabled software COMSOL was used for modeling. After careful grid variation, a total of 4436 triangular elements per half symmetry plane was chosen to represent tumor heating. The temperature tolerance was at the default value of 0.0001 and a direct matrix inversion technique was used.

Simulation of localized injected nanorod geometry using X-Ray tomography data

For the purpose of simulating the 3D geometry of injected nanorods and the resulting thermal flux upon irradiation, a multi-step procedure was performed to translate 3D X-ray CT images into a form amenable to computational modeling of photothermal heating. For the present cases, 406 DICOM slices were exported, including the tumor, muscle, and the internal skeletal details, as well as the distribution of injected nanorod solutions as shown in Fig. 3 and supplementary Figs. 5 and 6. Subsequently these data were imported in the image processing software Scan IP and reconstructed based on the grey scale values of the scan to form volumetric geometries for nanorods, skeletal structures, and soft tissues as shown in Fig. 3D supplementary Figs.5C and 6B. Next, the solid model was imported to the meshing software Scan FE and proper surface meshing was carried out. Finally, the 3D meshed geometries were imported to COMSOL Multiplysiscs and the thermal analysis was carried in an identical fashion to the previous description in the ellipsoidal geometry.

Results and discussions

Together, the data presented in Figs. 3, 4, S5, and S6 provide considerable evidence that the strategy of utilizing nanoantenna biodistribution data to empower computational irradiation regimen design has the potential to benefit the understanding of nanoantenna function *in vivo*. Particularly, given the large

number of uncertainties in biological systems with respect to parameters such as the precise delineation of underlying muscular tissues, the temperature dependence of thermophysical properties of tissues, variable blood perfusion, and precise tumor geometries (for intravenous cases), it is promising that prediction of the model is kinetically and quantitatively similar to measurements over the given range of parameters. The current work also motivates the future use of 3D methods for temperature measurement *in vivo*, such as the use of MRI. Efforts to integrate controlled NIR-irradiation conditions with MR imaging are beginning and will surely empower future improvements in model optimization.

It is additionally worth discussing the biophysical tissue characteristics that assist in focusing thermal energy within the tumor volume. Particularly, the blood perfusion rates in tumor and normal tissue are enhanced (although with different magnitudes) with increased tissue temperatures up to approximately 45^0C, allowing more efficient heat dissipation for moderate thermal gradients (Fujita et al., 1998). However, beyond 45^0C, tumor blood perfusion drops precipitously, causing tumoral heat dissipation to be diffusion limited. Meanwhile the thermal enhancement of peripheral tissue perfusion by up to 9-fold (see equations for w_b) allows more efficient peripheral cooling. These effects (internal tumor vessel shutdown and enhanced peripheral cooling) work in concert to focus the thermal accumulation within the tumor tissue and amplify the heating specificity imparted by the targeted nanoantennas. These effects will be directly investigated in future work using techniques that enable perfusion measurement during irradiation.

References

Fujita S., M.Tamazawa and K. Kuroda, *IEEE Trans. Biomedical Engg* , 1998, 45, 1182-1186.

Jain P.K., K.S. Lee, I.H.El-Sayed and M.A.El-Sayed, *J.Phys.Chem.B* ,2006,110,7238-7248.

Motamedi M. , T.J White and A.J. Welch , Laser Inst. Amer. ,Los Angeles, CA,1983.

Peennes H.H., *J. Appl. Physiology*, 1948, 1, 93- 122.

Welch A.J., *IEEE J. Quantum Electronics,* 1984, 20,1471-1481.